Journal of
Synchrotron Radiation

ISSN 0909-0495

Received 22 January 2009
Accepted 25 April 2009

High-energy X-ray diffraction using the Pixium 4700 flat-panel detector

J. E. Daniels[a]* and M. Drakopoulos[b]

[a]ID15, European Synchrotron Radiation Facility, Grenoble, France, and [b]I12, Diamond Light Source, Oxford, UK. E-mail: jdaniels@esrf.fr

The Pixium 4700 detector represents a significant step forward in detector technology for high-energy X-ray diffraction. The detector design is based on digital flat-panel technology, combining an amorphous Si panel with a CsI scintillator. The detector has a useful pixel array of 1910 × 2480 pixels with a pixel size of 154 µm × 154 µm, and thus it covers an effective area of 294 mm × 379 mm. Designed for medical imaging, the detector has good efficiency at high X-ray energies. Furthermore, it is capable of acquiring sequences of images at 7.5 frames per second in full image mode, and up to 60 frames per second in binned region of interest modes. Here, the basic properties of this detector applied to high-energy X-ray diffraction are presented. Quantitative comparisons with a widespread high-energy detector, the MAR345 image plate scanner, are shown. Other properties of the Pixium 4700 detector, including a narrow point-spread function and distortion-free image, allows for the acquisition of high-quality diffraction data at high X-ray energies. In addition, high frame rates and shutterless operation open new experimental possibilities. Also provided are the necessary data for the correction of images collected using the Pixium 4700 for diffraction purposes.

Keywords: high-energy X-rays; flat-panel detector; Pixium detector; diffraction; large area detectors; detector noise; MAR image plate.

1. Introduction

High-energy X-ray diffraction using large area detectors offers many advantages to other scattering techniques. The high-penetration depths and low scattering angles allow for complex sample environments to be constructed for *in situ* analysis while also providing true bulk structural information of the sample (Bohm *et al.*, 2003; Daymond & Withers, 1996; Korsunsky *et al.*, 1998; Wanner & Dunand, 2000; Daniels, 2008; Jones *et al.*, 2008). A typical set-up for a monochromatic high-energy X-ray diffraction experiment is shown in Fig. 1. The use of large area detectors to collect the full Debye–Scherrer cones in the forward direction greatly enhances the possible speed of data acquisition over conventional energy experiments (Chupas *et al.*, 2003).

While synchrotron storage ring and insertion device technology has greatly enhanced the available flux provided to experimental stations, the poor absorption efficiency and lack of technological development in high-energy detectors has meant that the vast majority of this flux is not utilized. A typical example of this inefficiency at beamline ID15 at the European Synchrotron Radiation Facility (ESRF) is an experiment whereby a good scattering sample only requires a detector image plate, such as the MAR345, be exposed for a few hundred microseconds, yet the readout of this image (including erase cycle and control macro completion) requires approximately 90 s. Such experiments have been commonplace at high-energy beamlines around the world for some time.

Of course, many fast area detector options are available, including coupling of image intensifiers, or scintillation screens

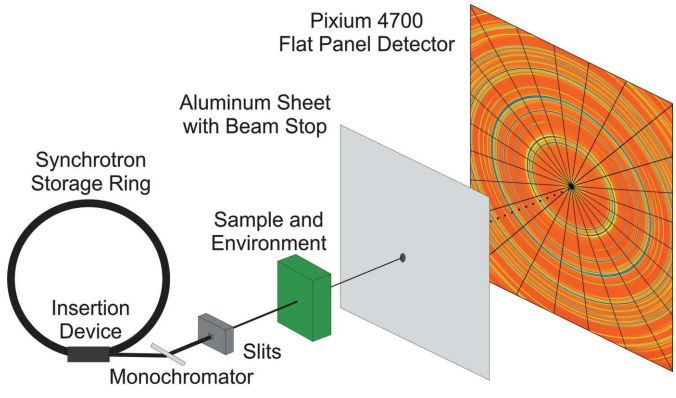

Figure 1
Typical set-up for high-energy X-ray diffraction at ID15B of the ESRF. The aluminium plate acts to filter low-energy fluorescence X-rays. The detector image shown is of a textured zirconium alloy; lines on the image indicate the possible 'caking' approach to data analysis allowing anisotropic effects to be examined in a single geometry.

Table 1
Pixium 4700 detector specifications.

Active area	381.9 mm × 294.1 mm
Useful pixel array	2480 × 1910
Pixel size	154 μm × 154 μm
ADC resolution	14 bits
Acquisition rate	7.5 Hz full frame
	30 Hz 2 × 2 binning
	Up to 60 Hz with selected region of interest
Cooling	Closed cycle water
Overall dimensions	478 mm × 366 mm × 85 mm
Weight	20 kg

with taper optics, to fast CCD or CMOS cameras (Gruner *et al.*, 2002). However, generally speaking, many of these systems suffer from variable image distortions, low resolution and/or small detection areas. Recently, a high-quality large area detector developed by GE has been demonstrated for diffraction purposes by the Advanced Photon Source (Lee *et al.*, 2007; Chupas *et al.*, 2007). This detector operates on very similar technology to the Pixium 4700 (Thales Electron Devices, 38430 Moiron, France). In the past ten years, however, by far the most successful large area detector to be used for high-energy X-ray diffraction is the MAR345 image plate scanner. This detector has a circular active area of diameter 345 mm with a pixel size of 150 μm × 150 μm or 100 μm × 100 μm (depending on the readout mode) and provides very high quality data. However, it is approximately 10% efficient at a photon energy of 90 keV, and requires close to 90 s to read out each image. The Pixium 4700 detector will be compared more closely with the MAR345 in §3.4.

The key features of the Pixium 4700 detector are outlined in Table 1. Throughout the remainder of this paper we will present and discuss more closely the properties of the detector in relation to conducting high-energy X-ray diffraction experiments. A detailed account of detector properties of interest to those working in the field of detector physics is not intended.

2. Experimental set-up

Tests of the detector were carried out at beamline station ID15B of the ESRF. A monochromatic beam of 87.7 keV was generated by a single-bounce Si(511) bent Laue monochromator. The beam size was then defined by a set of tungsten slits shortly before the sample stage. A schematic of this type of set-up is shown in Fig. 1.

3. Detector analysis

3.1. Ghost images

Image memory effects can introduce significant difficulties into the data analysis of diffraction images. In order to avoid erroneous results in highly precise measurements, the image decays must be known and accounted for. The Pixium 4700 detector (as well as other models from Thales) is equipped with a 'reset light', which effectively acts to clear the previously recorded image from the amorphous silicon charge collection element prior to exposure of the subsequent image. The duration of the reset light may be adjusted from 1 μs to 1000 μs and affects the decay properties. We found that, since ghost image behaviour is so critical to diffraction data analysis, there is no reason not to use the maximum reset light duration.

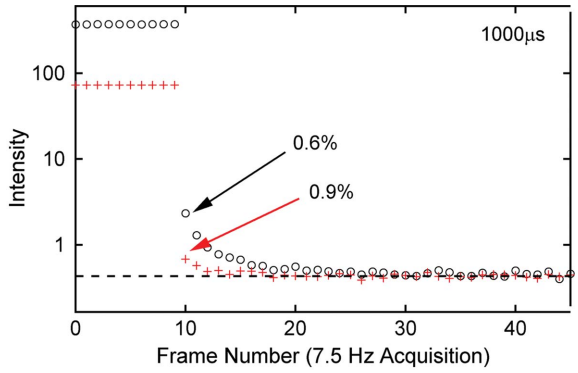

Figure 2
Ghost image decay as a function of frame number at 7.5 Hz acquisition for a reset light duration of 1000 μs.

We have measured the ghost image decay at the maximum reset light duration. The method of measurement was to expose the detector with a powder diffraction pattern while collecting images at a rate of 7.5 Hz and exposure time of 30 ms. During the acquisition a fast shutter was triggered such that the incident beam was cut between image frames. The subsequent images were then analysed for intensity decays. The results of these measurements are shown in Fig. 2.

With a reset light pulse of 1000 μs, the intensity in the first ghost image is found to be 0.6% and 0.9% for high and low pixel intensities, respectively. A residual intensity level of 0.1% is achieved after approximately ten additional acquisition processes. Such a low residual image effect is an excellent property, and for the majority of experiments this can be ignored completely. The behaviour of saturated pixels has not been analysed here, however, as with several detector systems it is recommended that saturated pixels be removed from data analysis for several images following the saturated image. The image decay properties presented here are a global average of pixels within certain intensity levels; however, this behaviour appears to be uniform across the entire detector area.

3.2. Point-spread/resolution

A measurement of the point-spread properties (or modulation transfer function, MTF) of both the Pixium 4700 and MAR345 detectors has been obtained by passing a direct beam of 50 μm × 50 μm (Pixium 4700) and 25 μm × 25 μm (MAR345) into the detection area. The beam energy for the MAR345 measurements was 80 keV. The results are shown in Figs. 3(*a*) and 3(*b*) for the MAR345 and Pixium 4700, respectively. The colour scale of the image plots is set to 10^{-2} of the maximum pixel intensity; this highlights qualitatively the superior point-spread behaviour of the Pixium 4700. It can be seen from the profile plots, shown in log scale, that the tails of the peak for the Pixium 4700 fall into the background level approximately seven pixels away from the centre. For the

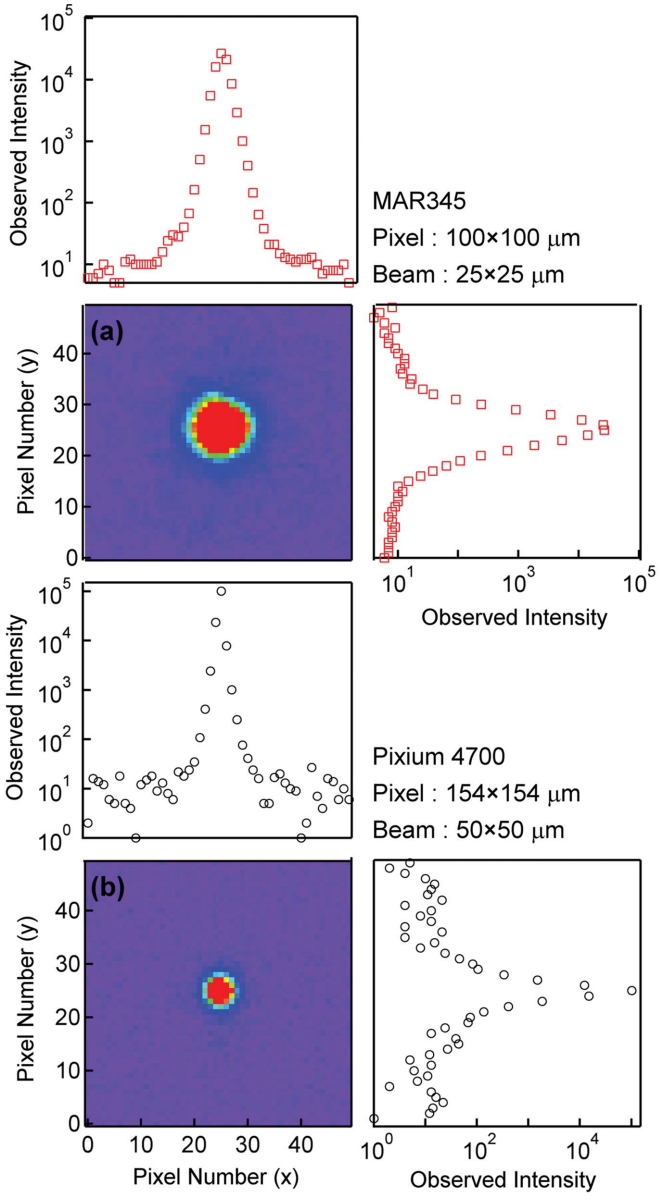

Figure 3
50 × 50 pixel region around a point beam incident on the MAR345 image plate (*a*) and the Pixium 4700 flat panel (*b*). In both images the colour scale maximum is 10^{-2} times the maximum intensity. The profile plots are on a logarithmic scale.

MAR 345 this value is close to 15 pixels. Both intensity profiles were fit using two-dimensional pseudo-Voigt functions; the full width at half-maximum was found to be 1 pixel and 2.8 pixels for the Pixium 4700 and MAR345, respectively. It should be noted, however, that the pixel size of the MAR345 during this test was 100 μm × 100 μm.

The result of such a narrow point-spread function is that very high resolution diffraction data are obtainable, particularly at high q values. Fig. 4 shows a diffraction image collected on the Pixium 4700 detector from an α-Fe powder. The exposure time is 0.4 s. The image obtained is radially integrated in the section outlined. Diffraction intensity as a function of scattering vector, q, is then plotted, with the inset showing the statistics and resolution available at very high q.

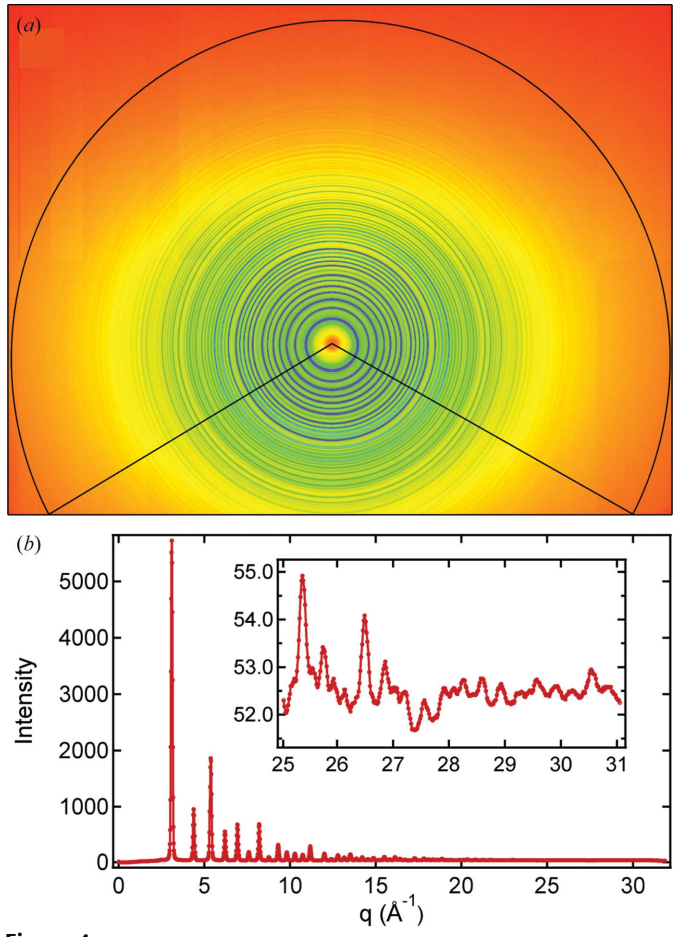

Figure 4
Example of a powder diffraction pattern collected from α-Fe during a 0.4 s exposure (*a*). The radially integrated pattern from the indicated region (*b*) shows good peak statistics to q-values in excess of 30 Å^{-1}.

By combining high resolution at high q values with the timing capabilities, the potential for rapid pair distribution function data acquisition is greatly enhanced from image plate and scanning detector systems (Chupas *et al.*, 2003; Egami & Billinge, 2003).

3.3. Attenuation and other corrections

Within this section, Pixium detector specific corrections are presented. More general corrections such as geometrical corrections to intensities are not provided as they are generally implemented in two-dimensional diffraction data reduction analysis packages, such as *fit2d* (Hammersley *et al.*, 1996).

The two primary effects which must be taken into account are the change in absorption lengths as a function of 2θ, and the change in probability of the scintillation photons reaching the detection elements as a function of depth. These are highlighted in Fig. 5. Both of these effects contribute to a difference in observed intensity and position, particularly at high 2θ values. In addition to these effects is the absorption of X-rays in the materials preceding the CsI detection element.

The exact compositions and densities of detector elements remain the proprietary information of Thales and thus cannot be quoted here. However, we have obtained this information

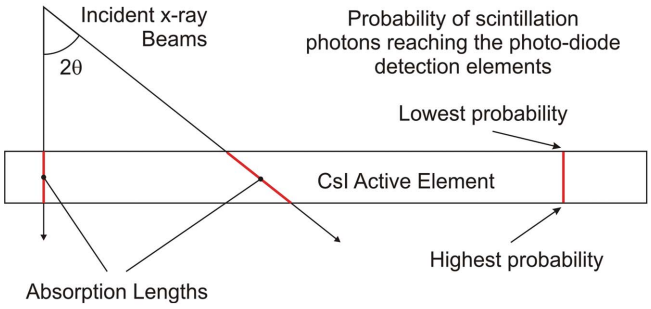

Figure 5
Factors influencing observed intensity.

(Thales, private communication) for use in the following calculations which will be sufficient for others to perform their own corrections for specific detector/beam-energy arrangements.

3.3.1. Intensity. The observed intensity as a function of 2θ can be calculated relative to a unit incident intensity by integrating the absorbed dose through the CsI active layer accounting for the scintillation efficiency as a function of depth; this is given by

$$I(2\theta, E) = \int_0^d G(x)\frac{\mu(E)}{\cos(2\theta)}\exp\left[-\frac{\mu(E)x}{\cos(2\theta)}\right]\mathrm{d}x, \qquad (1)$$

where $G(x)$ is a function describing the efficiency of the scintillator as a function of depth x, $\mu(E)$ is the linear attenuation coefficient at energy E, and d is the thickness of the scintillator. The density and compositional information required for calculation of $\mu(E)$ and $G(x)$ have been obtained from the manufacturers (Thales, private communication). Here we provide the relative intensity increases which need to be accounted for as a function of 2θ, normalizing to $2\theta = 0$; this is shown in Fig. 6. At low energies the effect is almost negligible, as approximately all of the incident beam is attenuated by the scintillator. However, upon increasing the energy the effect becomes much greater and must be accounted for.

The X-ray attenuation in all materials prior to the CsI active element must be taken into account and the observed intensities adjusted accordingly. During an experiment, this includes not only the detector materials but also the air gap and any other filtering materials (such as the Al sheet shown in Fig. 1). Here the correction for the detector materials only is given, and can be calculated using,

$$I_{\mathrm{final}} = I_{\mathrm{corr}}/\exp\left[-\frac{\mu(E)d}{\cos(2\theta)}\right], \qquad (2)$$

where I_{corr} is the intensity data after the corrections of oblique incidence given above, and $\mu(E)d$ is given in Fig. 7. The magnitude of this correction is very small and does not need to be accounted for during low-angle or very high energy experiments.

3.3.2. Position. The centre of mass of absorbed intensity changes as a function of angle and thus affects the observed 2θ positions at high angles. Fig. 8 highlights this effect. Here the

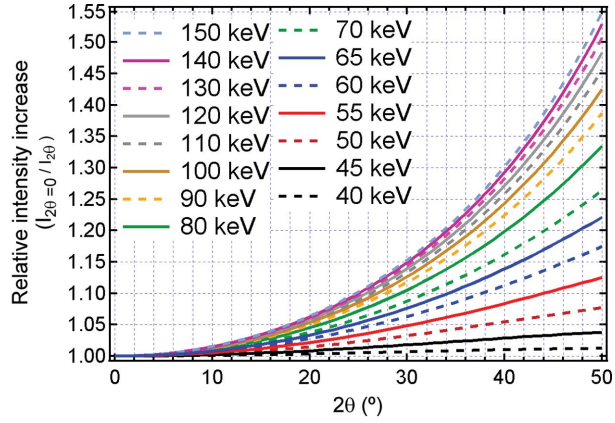

Figure 6
Relative intensity increase as a function of 2θ for selected energies in the specified operating range.

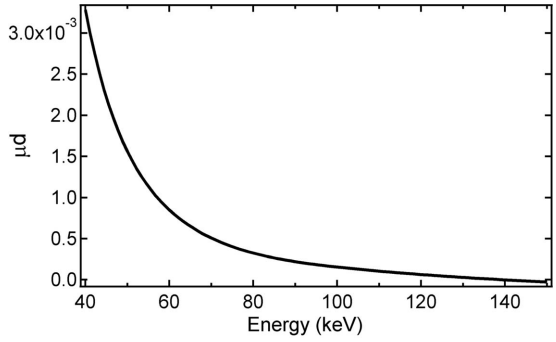

Figure 7
Linear attenuation coefficient multiplied by the thickness of the pre-scintillator materials of the Pixium 4700 detector.

observed intensity profile through the scintillator thickness is plotted for both $2\theta = 0$ and $2\theta = 50^\circ$, calculated at an incident energy of 50 keV. The centre of mass of these two deposited profiles is indicated. This difference corresponds to an effective change in distance between the sample and detector plane as a function of 2θ. Fig. 9 displays the Δd values (using $2\theta = 0$ as reference) for the Pixium 4700 detector for selected energies within its operating range. An interesting effect to note here is how the Δd value is passing through its maximum influence at an energy of 50 keV. At very low energies the

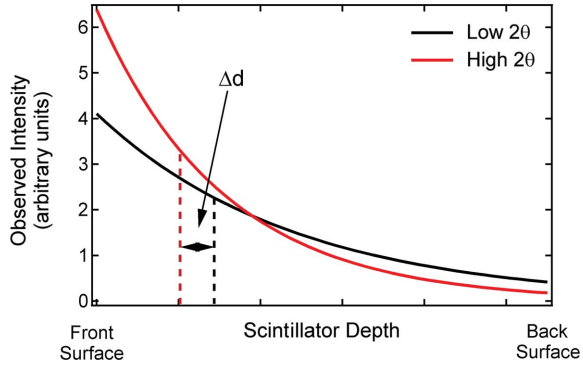

Figure 8
Change in the centre of mass of the observed intensity at two 2θ values. Profiles were calculated for the Pixium 4700 at an incident energy of 50 keV.

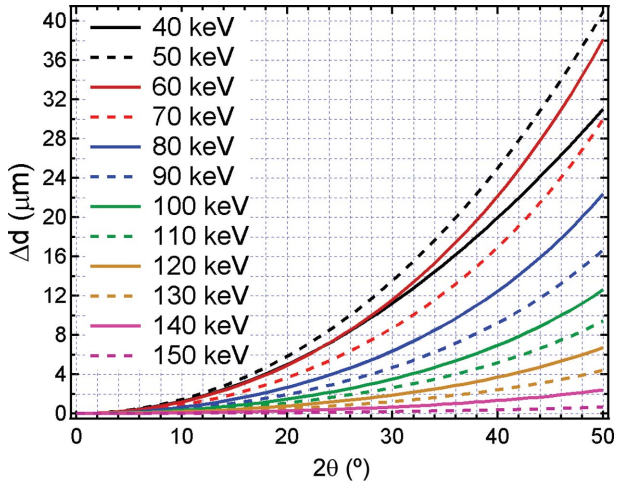

Figure 9
Change in the centre of mass of the observed intensity as a function of 2θ for selected energies within the operating range of the Pixium 4700 detector.

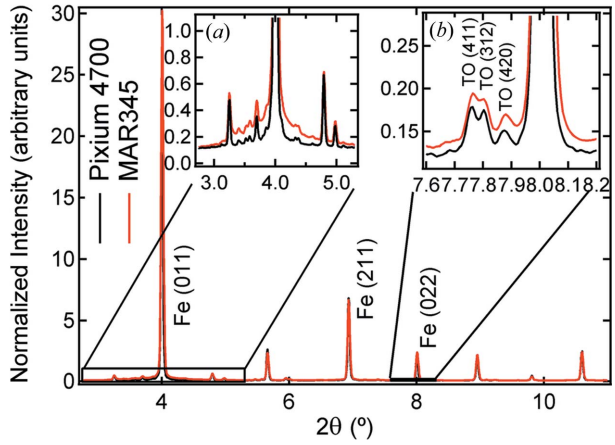

Figure 10
Radially integrated diffraction patterns recorded from the MAR345 image plate and Pixium 4700, normalized to equal intensities. (*a*) Broadening effect caused by MAR345 point spread function; (*b*) difference in resolution for selected doublet. Selected reflections from the Fe and TiO_2 (TO) phases are indicated.

majority of intensity is absorbed close to the front surface, thus Δd as a function of 2θ is very small. At very high energies, very little of the incident intensity is absorbed, thus the centre of mass is always in the centre of the detection element and Δd is again very small. The influence of Δd is generally quite subtle and in most cases may be neglected from the data analysis process. However, during high-q crystalline diffraction, *e.g.* crystalline PDF measurements, the correction may be advantageous.

3.4. Comparison with MAR345 image plate scanner

Diffraction data have been collected using both the Pixium 4700 flat-panel detector and the MAR345 image plate scanner (using 150 μm × 150 μm pixel size) under identical experimental conditions for the purposes of comparison. The sample chosen was a combination of body-centred cubic (b.c.c.) Fe (strong scatterer) and a TiO_2 sample (weak scatterer), in order to give a range of Bragg peak intensities to observe. Fig. 10 shows qualitatively the differences in diffraction patterns recorded from the two systems. Here an azimuthal wedge of 30° was integrated from the two detector images. Inset (*a*) highlights the increased peak tail intensity of the MAR345 as opposed to the Pixium 4700. Around strong Bragg peaks the intensity of the Pixium 4700 falls very rapidly owing to its very narrow point-spread function, which includes only short tails (see §3.2). The MAR345, however, has much broader tails within its point-spread function, thus the observed Bragg peak tails are also much broader. Inset (*b*) shows the improved resolution obtained using the Pixium 4700; Bragg peaks across the pattern have a consistently narrower full width at half-maximum and small doublet peaks are well resolved.

The absorption efficiency of the X-ray detection elements for the MAR345 and Pixium 4700 are calculated to be 10% and 30%, respectively, at an energy of 90 keV. This, however, is not a good measure of the image quality as noise issues are the key feature which will determine the final diffraction image statistics.

To quantitatively compare the image statistics from the two detectors is difficult, as they have different encoding accuracies, *i.e.* 16-bit for MAR345, 14-bit for Pixium 4700. This is not, however, a disadvantage for the Pixium 4700. Owing to its rapid readout time, multiple frames can be averaged in order to improve data quality.

We recorded a sequence of 100 diffraction images from a sample containing b.c.c. Fe (strong scatterer) and TiO_2 (weak scatterer). Each pattern was taken with an exposure time of 0.4 s, where the maximum intensities in the images were close to the full dynamic range of the detector. After the sequence was recorded, we calculated the arithmetic mean of a number of n images, where n was varied from 1 to 100. Fig. 11, insets (*a*) to (*f*), show such averaged images for n = 1, 2, 3, 5, 10 and 50 (only a region of the image is depicted). It can be seen with

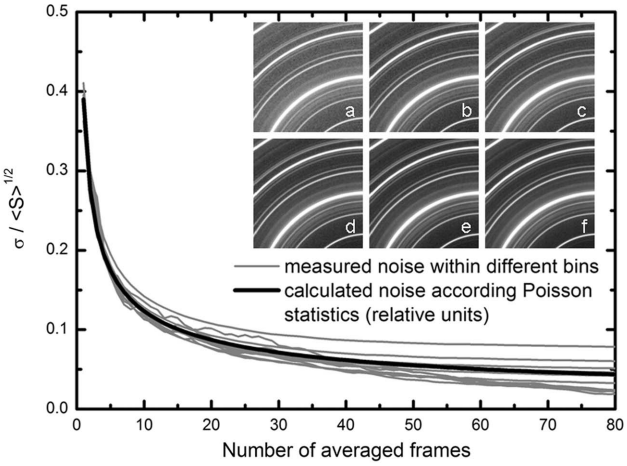

Figure 11
Standard deviation for averaged diffraction images. Standard deviation divided by the square root of the mean intensity for different intensity levels (grey lines). Calculated standard deviation for input signal following Poisson statistics (black line). Insets (*a*) to (*f*): selected area of diffraction images representing the average of 1, 2, 3, 5, 10 and 50 images.

the eye that a dramatic improvement in data quality is achieved as more images are averaged.

Averaging over n images increases the number of statistical events by n and divides the resulting signal by the same number. For an input signal following Poisson statistics, thus, the standard deviation σ of an averaged image is given by $(\Sigma_n \langle S \rangle_n)^{1/2}/n = \langle S \rangle^{1/2}/n^{1/2}$, where $\langle S \rangle^{1/2}$ is the standard deviation at the input. Therefore, the statistical noise in the averaged image decreases as $1/n^{1/2}$. Fig. 11 shows the measured ratio $\sigma/\langle S \rangle^{1/2}$ for different signal intensities (bins). The agreement with the expected $1/n^{1/2}$ behaviour is depicted too.

Systematic image deviations on a pixel-by-pixel basis have been observed to be minimal. There are, however, variations in the gain correction of the different readout segments of the detector; the detector contains in total of 44 separate readout sections. This gain variation is also minimal and of the order of 1%. This gain variation changes slowly over long time scales (months), and is recalibrated by uniform exposure of the detector area.

4. Conclusions

The Pixium 4700 flat-panel detector provides a significant step forward in detector technology for high-energy X-ray diffraction purposes. The combination of good absorption efficiency, rapid data readout times and high spatial resolution overcomes several drawbacks of previously available high-energy detectors. We have demonstrated the use of the Pixium 4700 detector for high-energy diffraction experiments, showing that it is superior to the MAR345 image plate system for experiments in which strong scattering signals are to be monitored, or time-resolved data are required. The opening up of new high-resolution time-resolved experiments offers many exciting opportunities for high-energy X-ray diffraction science.

The authors gratefully acknowledge the assistance of Laurent Claustre and Cyril Ponchut of the ESRF beamline software support and instrument support groups for their assistance in integration of the detector into beamline infrastructure. We also acknowledge the assistance of staff at Thales, X-ray Imaging Solutions, Components and Subsystems, Moirans, France. M. Di Michiel of ID15 is thanked for providing the MAR345 point-spread information and for valuable discussions on the topics presented.

References

Bohm, J., Wanner, A., Kampmann, R., Franz, H., Liss, K. D., Schreyer, A. & Clemens, H. (2003). *Nucl. Instrum. Methods Phys. Res. B*, **200**, 315–322.

Chupas, P. J., Chapman, K. W. & Lee, P. L. (2007). *J. Appl. Cryst.* **40**, 463–470.

Chupas, P. J., Qiu, X., Hanson, J. C., Lee, P. L., Grey, C. P. & Billinge, S. J. L. (2003). *J. Appl. Cryst.* **36**, 1342–1347.

Daniels, J. E. (2008). *J. Appl. Cryst.* **41**, 1109–1114.

Daymond, M. R. & Withers, P. J. (1996). *Scr. Mater.* **35**, 1229–1234.

Egami, T. & Billinge, S. J. L. (2003). *Underneath the Bragg Peaks, Structural Analysis of Complex Materials.* Oxford: Elsevier.

Gruner, S. M., Tate, M. W. & Eikenberry, E. F. (2002). *Rev. Sci. Instrum.* **73**, 2815–2842.

Hammersley, A. P., Svensson, S. O., Hanfland, M., Fitch, A. N. & Hausermann, D. (1996). *High Press. Res.* **14**, 235–248.

Jones, J. L., Pramanick, A. & Daniels, J. E. (2008). *Appl. Phys. Lett.* **93**, 152904.

Korsunsky, A. M., Wells, K. E. & Withers, P. J. (1998). *Scr. Mater.* **39**, 1705–1712.

Lee, J. H., Almer, J., Aydiner, C., Bernier, J., Chapman, K., Chupas, P., Haeffner, D., Kump, K., Lee, P. L., Lienert, U., Miceli, A. & Vera, G. (2007). *Nucl. Instrum. Methods Phys. Res. A*, **582**, 182–184.

Wanner, A. & Dunand, D. C. (2000). *Metall. Mater. Trans. A*, **31**, 2949–2962.